An analysis of directivity pulses using empirical data and dynamic rupture simulations of the 2023 Kahramanmaras earthquake doublet

Ming-Hsuan Yen[1, 2, *], Elif Türker[1,2], Thomas Ulrich[3], Mathilde Marchandon[3], Alice-Agnes Gabriel[3, 4], Fabrice Cotton[1, 2]

[1] German Research Centre for Geosciences, Potsdam, Germany

[2] University of Potsdam, Institute of Geosciences, Potsdam, Germany

[3] Department of Earth and Environmental Sciences, Ludwig-Maximilians-Universität München, Munich, Germany

[4] Institute of Geophysics and Planetary Physics, Scripps Institution of Oceanography, University of California San Diego, La Jolla, CA, USA

*Corresponding author: ming-hsuan.yen@gfz-potsdam.de

ABSTRACT

Near-field earthquake ground motions with strong velocity pulses have the potential to cause extensive damage to buildings and structures. Such strong velocity pulses have been identified during the Mw 7.8 and Mw 7.5 earthquake doublet of the 2023 Turkey seismic sequence and could have contributed to the dramatic damage extent. Therefore, better understanding and characterizing pulse properties (e.g., their period and amplitude) and their underlaying physical factors is crucial for the earthquake-resistant design. In this study, we characterize the velocity pulses of the observed records and of synthetic waveforms from a dynamic rupture simulation of the Mw 7.8 event. We observe significant variability in the pulse properties of the observed records in the near fault regions, particularly regarding orientations. This variability is not fully captured by the dynamic rupture simulation, which allow us constraining the variability controlling factors. Our results indicate that directivity effects are not the only factors influencing the

pulse characteristics in this earthquake doublet. While, site effects (e.g., the basin effect) may also influence the pulse characteristics for some stations, local heterogeneities in slip amplitude and orientations could be critical factors in generating or influencing the pulse properties in this earthquake doublet.

INTRODUCTION

The left-lateral East Anatolian Fault Zone (EAFZ) in Turkey, extends for more than 550 km, starting from the Karliova Triple Junction in the East to the southernmost end in the Mediterranean Sea (Duman and Emre, 2013). Although, the EAFZ is comparably less seismically active than the North Anatolian Fault Zone, it hosted numerous large (Mw > 6.5) earthquakes during the last centuries (Sengör et al. 1985; Tatar et al. 2004), with the last one being the Mw 6.8 Elazig earthquake in 2020.

On February 6, 2023, at 01:17 UTC, a Mw 7.8 earthquake nucleated only 20 km off the main strand of the EAFZ and ruptured multiple segments of the East Anatolian Fault system. Only 9 hours later, another major earthquake (Mw 7.5) occurred 90 km north of the first mainshock, on the northern strand of the EAFZ, near to the province of Elbistan. Following these two mainshocks, the region experienced hundreds of aftershocks with Mw > 4. In the following, we refer to these two major events as “earthquake doublet”. This doublet caused significant damage to more than 220,000 buildings (totally destroyed or collapsed) leading to more than 55,000 causalities in Turkey and Syria (Hacettepe University Department of Civil Engineering, 2023). Cities with an epicentral distance of more than 150 km (e.g., Hatay) were completely destroyed. Thus, it was the worst disaster that the country has suffered in the last millennium.

Strong velocity pulses have been identified in these earthquakes and have been correlated with the observed extensive damage distribution (Baltzopoulos et al., 2023; Erdik et al., 2023). These outcomes are in alignment with previous studies of large and moderate earthquakes that demonstrated the potential impact of strong velocity pulses on the resulting seismic damage (Heaton et al., 1995; Strasser and Bommer, 2009; Türker et al., 2023).

Such velocity pulses can be generated by two main physical phenomena: fling steps and directivity effects. A Fling step is associated with displacement waveform that contains a permanent offset and occurs in very near-surface fault ruptures (Hisada and Tanaka, 2021). It is characterized by a one-sided pulse (fling pulse) in the velocity waveform and a step-function displacement waveform. Directivity pulses result from near-field rupture directivity effects and are observed in the rupture propagation direction (Somerville et al., 1997; Bray and Rodriguez-Marek, 2004). A directivity pulse is characterized by a two-sided pulse in the velocity waveform. However, several studies have discussed that the origin of velocity pulses may be more complex. Rodriguez-Marek and Bray (2006) showed that site effects can interact with near-field directivity effects when the pulse period is close to the dominant frequency of the site. These effects may interact with one another or solely affect the pulse generations (Chioccarelli and Iervolino, 2010; Kaneko and Goto, 2022), potentially leading to a large variability in pulse properties.

Most pulse analysis have been undertaken, using empirical data. However, numerical simulations can also help to better assess the factors controlling the pulse variability (e.g., Yen et al., 2022). Indeed, the severe seismic damage and complex rupture process of this seismic sequence in Turkey has inspired numerous studies to understand the earthquake origin and rupture process (e.g., Jia et al. (2023), Mai et al. (2023), and Petersen et al. (2023)). The dynamic rupture models of Jia et al. (2023), which treat the nucleation, propagation and arrest of earthquakes in a physically self-consistent manner, independently reproduce the main features of the kinematic models for the Mw 7.8 earthquake and produce ground motion synthetics that show pulse-like behavior. These simulations then provide a valuable opportunity to study the variability of ground motion pulses from the synthetic data.

This study we perform a detailed analysis of the pulse variability in period, velocity amplitude and orientation. We use the wavelet analysis of Shahi and Baker (2014) (see the Methodology section) to extract the pulses and characterize their properties. To comprehensively quantify and evaluate pulse variability, we analyze the characteristics of the observed pulses and those obtained from the simulations of Jia et al. (2023). Furthermore, we compare the results with the pulse characteristics obtained in past earthquakes (updated database of Yen et al. (2022)).

DATA

For the analysis, we investigate two observed empirical datasets of the Mw 7.8 Pazarcik and Mw 7.5 Elbistan earthquakes and two synthetic datasets of the Mw 7.8 Pazarcik earthquake. The Mw 7.8 Pazarcik and Mw 7.5 Elbistan earthquakes were recorded by 349 and 288 strong ground motion stations (AFAD-TADAS), respectively. The two synthetic datasets are derived from the physics-based 3D dynamic rupture simulation of Jia et al. (2023).

The first observed empirical data used in this study are initially provided by AFAD-TADAS. We perform the following processing on the raw data: (1) detrending acceleration waveforms, (2) cumulative integration of acceleration waveforms into velocity waveforms, (3) detrending velocity waveforms. We refer to this dataset as "uncorrected data," which means that the static displacement in the time history is uncorrected.

The corrected data are provided by the Engineering Strong Motion Database, ESM (Luzi et al., 2020), which have been manually corrected by the ESM data processing team using the broadband ITACA processing schemes of Paolucci et al. (2011). (1) A baseline correction (constant de-trending), a cosine taper, and a 2nd order acausal frequency domain Butterworth filter is applied to the acceleration time series. (2) The double integration is applied to the acceleration time series to obtain the displacement time series. (3) Linear de-trending is applied to the obtained displacement time series. These processes remove the static displacements in the time history, as shown in the time histories of stations 3123 (in the basin), 3144 (at the center of the rupture fault), 4615 (near the hypocenter), and 4616 (at the intersection of two faults) shown in **Figure S1**. We refer to this dataset as "corrected data," which indicates that the static displacement in the time history is removed.

Two synthetic datasets used in this study are derived from the dynamic rupture simulation of Jia et al. (2023) and are referred to as the 1st synthetic data and the 2nd synthetic data. The 1st synthetic dataset is directly from the model of Jia et al. (2023), with a maximum resolved frequency of 1.5 Hz. The 2nd synthetic data is a higher resolution derived model, based on a larger mesh of 685 million cells, higher polynomial order of the basic functions p=5, and is numerically accurate to 5 Hz in a NW-SE aligned refined area of 400 x 200 x 20 km, which contains the fault network and all the near-fault stations). Dynamic rupture model requires many assumptions, including the fault loading and strength, velocity model, subsurface structure and geometry, and failure criterion. The fault geometry is based on the surface rupture traces inferred from available satellite inferences (e.g., USGS and Sentinel 2 inferences), and the initial shear stress is inferred from regional seismo-tectionics with small-scale heterogeneities inferred from static slip inversion. The models incorporate topography. The 1D velocity model is based on the study of Güvercin et al. (2022), and does not account for heterogeneous site configurations (e.g., Vs30). Such models predict the evolution of slip, seismic waves, and surface deformation in a physically self-consistent manner. The maximum resolved frequency is sufficient for our pulse identification analysis, since pulse periods are generally between 1 and 15s (0.1-1 Hz), as shown by the pulse scaling in Shahi and Baker (2014) and Yen et al. (2022). Jia et al. (2023) have shown that the surface displacements and slip histories produced by the dynamic rupture simulation compare well with the high-resolution geodetic data, kinematic rupture representations, and observed ground motions. We further examine how pulse characteristics and their variability are reproduced by the models. The synthetic time histories of selected stations are shown in **Figure S2**. The data processing on them is carried out in the same way as on the uncorrected data.

IDENTIFICATION AND CHARACTERIZATION OF VELOCITY PULSES

Methodology

In this study, we use the wavelet analysis algorithm of Shahi and Baker (2014) to detect the pulse-like velocity in Kahramanmaraş earthquake doublet. Their wavelet analysis is widely recognized, as used in other studies on this earthquake doublet (e.g., Baltzopoulos et al., 2023; Ertuncay and Costa, 2024). In addition, this choice ensures consistency in the characterization of velocity pulses with previous studies, particularly the analyses of Shahi and Baker (2014) and Yen et al. (2022), we apply this wavelet analysis algorithm.

The algorithm uses the wavelet transform of two horizontal orthogonal components of the ground motion to search for orientations that are more likely to contain strong pulses. The wavelet with the largest coefficient, is identified as the strongest pulse. Thus, the pulse properties in this study indicate the pulse properties of the strongest pulse.

The strength of a pulse is classified by the pulse indicator (PI), which defines the strength of the pulse as Equation 1 (Equation 12 of Shahi and Baker, 2014):

$$PI = 9.384(0.76 - PC - 0.0616PGV)(PC + 6.914 \times 10^{-4}PGV - 1.072) - 6.179$$

$$PC = 0.63 \times PGV_{ratio} + 0.777 \times energy_{ratio} \quad (1)$$

in which the principal component (PC) is the linear combination of two variables (peak ground velocity of the waveform projected along the extracted orientation [PGV] ratio and energy ratio), accounting for the largest amount of variability in the data, and the energy ratio is the energy ratio (L2 norm) of residual and original ground motions, and the PGV ratio is the ratio of the residual and original PGV.

As a first criterion for pulse identification, the peak ground velocity (PGV) must be greater than 20 cm/s which referred to the criterion of Shahi and Baker (2014). The classification algorithm then categorizes a velocity time history as either pulse-like or non-pulse-like according to the PI value. Accordingly, a record is defined as pulse-like if PI > 0, or as non-pulse-like if PI < 0. The algorithm also provides additional information about the pulse, including the pulse orientation, the associated peak ground velocity (PGV), and the pulse period (T_p).

Velocity pulses from observed empirical data

Following the selection criteria mentioned above (i.e., PGV > 20 cm/s), 50 stations within a rupture distance (R_{rup}) of 250 km were selected for both the observed data (uncorrected and corrected) for the Mw 7.8 Pazarcik earthquake. Similarly, 21 stations within a rupture distance of 200 km were selected for the observed data for the Mw 7.5 Elbistan earthquake. The identified pulses from the corrected data of the Pazarcik earthquake (1st event) are present at 23 out of the 50 stations listed in **Table 1**. The pulses identified for the Elbistan event (2nd event) are listed in **Table 2**, with 7 out of the 21 stations being indicated as pulses. The rupture distances are calculated from the stations to the rupture models of the earthquake doublet referenced by the United States Geological Survey (USGS).

Figure 1a and **Table 1** show the pulse distribution for the observed data of the Mw 7.8 Pazarcik earthquake (1st event). A noticeable trend is that the majority of the observed pulses are almost all located on the main fault branch (EAFZ), with 22 out of 23 records having R_{rup} < 20 km (i.e., near-fault). On the other hand, the hypocentral distances seem to play a minor role in pulse detection, with highly variable distances ranging from 30 km up to 130 km (**Table 1**). The pulse orientations (i.e., fault-normal (FN) or fault-parallel (FP) component) show a high variability. The largest pulse PGV (173-179 cm/s) is found at station 3123, which is located in the city of Antakya (R_{hyp} = 130 km; R_{rup} = 1.5 km), the city that suffered the most in terms of seismic damage during these events.

Figure 1b and **Table 2** show the pulse characteristics for the observed data of the Mw 7.5 Elbistan earthquake (2nd event). It is noticeable that the pulses are mostly located to the south, away from the main fault segment with the R_{rup} ranging from 3 km up to almost 70 km. Pulse-like features are detected only at a few stations and at greater distances. This may be due to the fact that the limited stations near the fault. Pulse orientations at the stations in the rupture direction are on the FN component (stations 131, 132 and 4612), and those at the stations to the south of the fault are on the FP component. The largest pulse PGV (181 cm/s) is at station 4612, which is marked by R_{rup} = 3 km.

Velocity pulses from synthetic data

First, to ensure that the synthetic recordings exhibit the key features of interest, we compare the time histories of stations 3123 (in Karasu-Amik Basin), 3144 (at the center of East Anatolian Fault), 4615 (near the hypocenter), and 4616 (at the intersection of East Anatolian Fault segments) for the uncorrected, corrected, and synthetic data (**Fig. 2**). All of their time histories show pulse-like features, which confirms that we can analyze the pulses with the help of these synthetic data.

We then apply the pulse extraction algorithm to both generations of the synthetic ground motions. The synthetic data of the Pazarcik event show pulse-like features at 18 out of 50 stations in the 1st synthetic data, and at 17 out of 50 stations in the 2nd synthetic dataset (**Table 1**). The simulations are able to capture specific pulse characteristics, such as the pulse period and velocity, at most stations in the near-fault region. However, the pulse orientations show a significant tendency to focus primarily on the FN component in both synthetic data (**Figs. 3a and 3b**).

Understanding the variability of pulse orientations

Somerville et al. (1997) showed that the pulse can be present in two horizontal orthogonal components associated with two different phenomena (directivity effects and fling-step) and can also overlap in some orientations. However, the static displacements are removed in the corrected data and the fling-step effect is therefore excluded from this dataset. Again, it should be noted that the pulse orientation here indicates the orientation of the strongest pulse, so it represents the most dominant effect.

Figure 4 shows a comparison of pulse orientations and their uncertainty from the uncorrected, corrected data and 1st synthetic data. The within-pulse uncertainty in orientations range between 20 to 30 degrees in both observed and synthetic data. The orientations between pulses show a high variability in the observed data. However, the orientations of the synthetic data show that the pulses are predominantly aligned with the FN component, with less variability compared to the pulses from the observed data.

A common statement is that near-field rupture directivity effects generate pulses in the FN component (Somerville et al., 1997; Bray and Rodriguez-Marek, 2004; Kaneko and Goto, 2022). However, the pulse orientations of these two events are highly variable, as shown in **Fig. 5a**. The pulse orientations of the Pazarcik earthquake are highly variable in the near-fault region (R_{rup} < 5 km), but become more pronounced in the FN component for stations with R_{rup} > 5 km. At far distant stations (R_{rup} > 30 km) the pulse orientations for the Elbsitan earthquake are almost all observed on the FP component. The observed pulses in this earthquake doublet show that a large variability of the pulse orientations.

This large variability in pulse orientation may not solely occur due to directivity effects. Site-effects (e.g., basin and soft-soil effects) may also influence the detected velocity pulses (Kobayashi et al., 2019). To analyze the site effect in this matter, we evaluate the correlation between the pulse orientations and the corresponding Vs30 (a proxy for the site conditions) (**Fig. 5b**). A few pulses are observed at stations with low Vs30 (soft soils, Vs30 < 360 m/s). For these stations pulses shown on the FP component may then be a consequence of the site effects (e.g., NAR). Ground motion pulses on soft soils would exhibit multiple large cycles in the time history, which is generally a signature of the presence of soft-soil effects (Somerville, 2003). The ground motion at station 3123 (Vs30 = 470 m/s) in the Pazarcik earthquake (showing a pulse-like feature) shows such multiple large cycles (**Fig. 5c**). However, the correlation between pulse orientation and Vs30 remains weak, and most of stations showing pulses are located on stiff soils. This suggests that other factors (see Discussion) may explain the variability in orientation.

Comparison of the velocity pulses with a global dataset

In **Figure 6**, we compare the pulse periods extracted from the corrected data of this earthquake doublet with previously observed pulse periods of global earthquakes (Shahi and Baker, 2014; Yen et al., 2022; Türker et al., 2023). These observations of earthquake pulses show a correlation between pulse period and earthquake magnitude, and a large within-event variability of the pulse period for a single earthquake (various records of a single earthquake), as shown in Yen et al. (2022). The pulse periods observed in the Mw 7.5 Elbistan earthquake are comparable to those of the Mw 7.6 1999 Kocaeli earthquake. The standard deviation (log transformation) of the pulse periods of the Mw 7.8 Pazarcik earthquake (1.19) is larger than that of the pulse periods of the Mw 7.5 Elbistan earthquake (0.64). This is in agreement with the study of Yen et al. (2022) which showed that the within-event variability of the pulse period is magnitude-dependent (see Discussion).

Since previous studies have shown that the pulse period is not simply related to the earthquake magnitude (e.g., Yen et al., 2022), we further analyze the correlation of the pulse period and PGV with the rupture distance, which is one of the dependencies of this large within-event variability (**Fig. 7**). The pulse periods of the two events range from 3 s up to 14 s at different distances, suggesting no particular dependence between rupture distance and pulse period.

In **Figure 7b**, we compare the pulse PGV with the predicted PGV from the ground motion model of Bindi et al. (2014) for the Mw 7.8 earthquake with a selected Vs30 = 480 m/s. The ground motion model of Bindi et al. (2014) is derived for Europe and the Middle East from the RESORCE strong motion database, which does not consider directivity effects. Noteworthy, the predicted PGV is the geometric mean of the horizontal components, and the pulse PGV is the peak value of ground velocity projected along the extracted orientation. In general, the pulse PGV is larger than the predicted PGV and around the upper bound of one standard deviation of the ground motion model predictions. In the near fault regions (R_{rup} < 5km) the largest pulse PGV reaches about 200 cm/s for the observations. This analysis confirms that the pulse PGV in the Pazarcik and Elbistan earthquakes are consistent with the values and decay with rupture distance shown by other earthquakes of similar magnitude.

Response spectra of pulse-like vs non-pulse-like recordings

While peak ground motion effectively represents the highest intensity of ground motion during an earthquake, it lacks the ability to understand the seismic response of structures that have distinct natural vibration periods, when subjected to near-fault pulse-like ground motions. It is precisely the amplitude and duration (T_p) of the seismic pulses that contribute to higher spectral displacement and might result in larger damage, depending on the structural behavior of the building (Günes and Ulucan, 2019). A critical parameter for the description of structural response is given by the ratio of the pulse duration, T_p, and the natural period of the building, also known as first mode period, T1. Previous studies have already demonstrated an expected wider shape in the acceleration response, when near-fault ground motions include velocity pulses (Chopra and Chintanapakdee, 2001). Accordingly, the possible effects of near fault pulse-like ground motions should be accounted for in PSHA studies, as suggested earlier by Shahi and Baker (2011).

Considering the destructive and widespread damage of the two major events, we analyze the pseudo-elastic response spectra (hereafter: response spectra) of several pulse-like and non-pulse-like recordings to evaluate the potential impacts of the detected velocity pulses on the seismic response of buildings. **Figure 8** shows the velocity response spectra of pulse-like and non-pulse-like near-field recordings taken at similar fault distances (R <

35 km). The difference in the shape of the response spectra as well as in the maximum values is significant among the stations, with noticeable broader and higher spectral values for pulse-like recordings (red curves in **Fig. 8a**). The pulse-like ground motion shakings are shifted to longer periods, with a larger destruction potential on modern thus tall buildings. This trend is more pronounced for the records of the Pazarcik event (Mw 7.8), as shown in **Figure 8a**. However, we emphasize that more stations are available for this event, in contrast to the Elbistan earthquake (**Fig. 8b**), where only a handful of near-fault recordings are available. Such results are consistent with the analysis of Ertuncay and Costa (2024).

DISCUSSION

In this study, we detect several velocity pulses near the ruptured fault segments (R_{rup} = 1- 70 km) that strongly affect the response spectral characteristics of the observed ground motions (**Fig. 8**). Comparisons of the pulse period and pulse velocity amplitude with other damaging earthquakes in the global datasets confirm that the pulses of these two events are not unexpectedly large and consistent with past observations (**Figs. 6 and 7**).

The pulses observed during the Mw 7.8 Pazarcik earthquake show a large variability in pulse characteristics, even when fling-step effects are excluded (**Fig. 1**). The occurrence of the pulses is highly specific to the station location. Indeed, the variation of the pulse properties remains significant even when the inter-station distance (D) is small (D < 5 km). For example, in the Pazarcik earthquake, stations 2708 and 2709 are close to each other (D = 3.8 km), but only the record of one of the two station was defined as pulse-like

(**Fig. 1**). There is a large difference in pulse orientation (73°) between station 4615 and NAR (D = 1.8 km) (**Table 1**).

In the empirical regressions of pulse period and earthquake magnitude, standard deviations are calculated for all events. For instance, in the study of Shahi and Baker (2014), the standard deviation of the log-transformed period is 0.57, which is assumed to be constant for all magnitudes. However, our results are inconsistent with this constant standard deviation for all magnitudes. We observe that the log-transformed standard deviation is 1.19 for the Mw 7.8 Pazarcik earthquake and 0.64 for the Mw 7.5 Elbistan earthquake. This is consistent with the finding of Yen et al. (2022) that the standard deviation of the pulse period is indeed magnitude-dependent. Large earthquakes may involve more complex physical phenomena, such as more heterogeneous slip and varied fault mechanisms, which may contribute to increased pulse variability. Consequently, this magnitude-dependent variability suggests the importance of further investigation into the driving factors of the pulse variability between earthquakes.

Due to their destructive nature, directivity pulses, have been the focus of several studies during the last decades. Somerville et al. (1997) showed that directivity pulses are often expected on the FN component for strike-slip earthquakes. However, Poulos and Miranda (2023) and Türker et al. (2023) have shown that the orientations of the maximum spectral response (i.e., pulse orientation) do not occur exclusively on the strike-normal orientation when considering stations recorded at different distances. The results of our study support these observations, as the two events show highly variable in pulse orientations, with no tendency to align only on the FN component (**Fig. 5**). The kinematic simulations (**Fig. S3**) shows that the pulse orientations strongly depend on the faulting mechanism and the relative location of the station to the fault in the near-fault region. This is consistent with the study of Poiata et al. (2017) which indicated that the pulses are not only influenced by directivity effects, but also by a combination of rupture configurations and the S-wave radiation pattern.

Furthermore, another interpretation is that the presence of directivity pulses is strongly related to slip heterogeneity on the fault plane, where the location and size of asperities (large slip areas) determine the generation of directivity pulses (Mena and Mai, 2011). Dreger et al. (2011) have simulated strong ground motions by a 3D finite-difference method and also found that segmented faults and short-wavelength variations in fault geometry can introduce complexity that can affect the degree of directivity focusing and also the FP motions. Their simulations show that both fling-steps and directivity pulses can occur in any of the three components and suggested that faulting style and variation in the fault parameters must be taken into account in detailed site-specific analysis. It may then suggest that the dynamic rupture simulation should consider more heterogeneous slip and fault mechanism complexity to reproduce the variability of pulse observations.

Some studies have also shown that the site effect can influence both the amplitude and the period of directivity pulses when the pulse period is close to the site resonance period (Kobayashi et al., 2019; Rodriguez-Marek and Bray, 2006). Our analysis of the pulse orientations and the correlation with Vs30 and the ground motion at station 3123 (**Fig. 5c**) confirms that the site effect, together with directivity effects, can affect the pulse characteristics, and specifically increase its amplitude. However, site effects are probably not the main controlling factors since the correlation with Vs30 remains weak (**Fig. 5**).

Other factors mentioned above (e.g., heterogeneous slip and complexity of the fault mechanism) may contribute more to the pulse variability in this earthquake doublet.

CONCLUSIONS

In this study, we show that the pulse characteristics in the near-fault regions of large-magnitude earthquakes can be highly variable, especially the pulse orientation, and that the within-event variability of the pulse period is magnitude-dependent, as found by Yen et al. (2022). This pronounced variability in pulse characteristics can be attributed to various factors (e.g., directivity, site, and source effects). We confirm that site effects can amplify the pulse amplitude when the pulse period is close to the site resonance frequency, e.g., at the station 3123 in the Mw 7.8 Pazarcik earthquake. However, site effects are not the main factor increasing the pulse variability. Our results also suggest that heterogeneous slip and more complex fault mechanism are major factors increasing pulse variability in large earthquakes, and that the interaction of these factors makes the pulse properties even more variable. The significant pulse variability resulting from the various driving factors emphasizes the importance of studying each earthquake individually to understand the factors that influence pulse characteristics.

DATA AND RESOURCES

Preliminary finite fault geometry from the USGS: M7.8 Pazarcik earthquake
“https://earthquake.usgs.gov/earthquakes/eventpage/us6000jllz/finite-fault” and
M7.5 Elbistan earthquake
“https://earthquake.usgs.gov/earthquakes/eventpage/us6000jlqa/finite-fault” (last

acc. 20/06/2023). ESM Ground motion records: https://esm-db.eu/ (last acc. 20/06/2023). The raw from AFAD: https://en.afad.gov.tr/ (last acc. 31/03/2023).

ACKNOWLEDGEMENTS

The author acknowledges two anonymous reviewers for valuable comments. The authors would like to convey appreciation to colleagues from the Disaster and Emergency Management Presidency (AFAD) of Türkiye for granting free access to the strong ground motion records.

REFERENCES

Ancheta, T. D., Darragh, R. B., Stewart, J. P., Seyhan, E., Silva, W. J., Chiou, B. S.-J., Wooddell, K. E., et al., 2014. NGA-West2 Database. *Earthquake Spectra*, **30**(3), 989–1005. DOI: 10.1193/070913EQS197M

Baker, J. W., 2007. Quantitative Classification of Near-Fault Ground Motions Using Wavelet Analysis. *Bulletin of the Seismological Society of America*, **97**(5), 1486–1501. DOI: 10.1785/0120060255

Baltzopoulos, G., Baraschino, R., Chioccarelli, E., Cito, P., Vitale, A., and Iervolino, I., 2023. Near-source ground motion in the M7.8 Gaziantep (Turkey) earthquake. *Earthquake Engineering & Structural Dynamics*, **52**(12), 3903–3912. DOI: 10.1002/eqe.3939

Bindi, D., Massa, M., Luzi, L., Ameri, G., Pacor, F., Puglia, R., and Augliera, P., 2014. Pan-European ground-motion prediction equations for the average horizontal component of PGA, PGV, and 5 %-damped PSA at spectral periods up to 3.0 s using the RESORCE dataset. *Bulletin of Earthquake Engineering*, **12**(1), 391–430. DOI: 10.1007/s10518-013-9525-5

Bray, J. D., and Rodriguez-Marek, A., 2004. Characterization of forward-directivity ground motions in the near-fault region. *Soil Dynamics and Earthquake Engineering*, **24**(11), 815–828. DOI: 10.1016/j.soildyn.2004.05.001

Chioccarelli, E., and Iervolino, I., 2010. Near-source seismic demand and pulse-like records: A discussion for L'Aquila earthquake. *Earthquake Engineering & Structural Dynamics*, **39**(9), 1039–1062. DOI: https://doi.org/10.1002/eqe.987

Chopra, A. K., and Chintanapakdee, C., 2001. Comparing response of SDF systems to near-fault and far-fault earthquake motions in the context of spectral regions. *Earthquake Engineering & Structural Dynamics*, **30**(12), 1769–1789. DOI: 10.1002/eqe.92

Duman, T. Y., and Emre, Ö., 2013. The East Anatolian Fault: geometry, segmentation and jog characteristics. *Geological Society, London, Special Publications*, 372(1), 495–529. DOI: 10.1144/SP372.14

Erdik, M., Tümsa, M. B. D., Pınar, A., Altunel, E., and Zülfikar, A. C., 2023, A preliminary report on the February 6, 2023 earthquakes in Türkiye, http://doi.org/10.32858/temblor.297

Ertuncay, D., and Costa, G., 2024. Analysis of impulsive ground motions from February 2023 Kahramanmaraş earthquake sequence. *Bulletin of Earthquake Engineering*. DOI: 10.1007/s10518-024-01897-x

Güneş, N., and Ulucan, Z. Ç., 2019. Nonlinear dynamic response of a tall building to near-fault pulse-like ground motions. *Bulletin of Earthquake Engineering*, **17**(6), 2989–3013. DOI: 10.1007/s10518-019-00570-y

Güvercin, S. E., Karabulut, H., Konca, A. Ö., Doğan, U., and Ergintav, S., 2022. Active seismotectonics of the East Anatolian Fault. *Geophysical Journal International*, **230**(1), 50–69. DOI: 10.1093/gji/ggac045

Hacettepe University Department of Civil Engineering, 2023. 06 February 2023 – Kahramanmaraş Pazarcık (Mw=7.7) and Kahramanmaraş Elbistan (Mw=7.6) Report on the Investigation of Earthquakes. *Hacettepe University Department of Civil Engineering Report*. URI: https://drive.google.com/file/d/1u8LYtSvkks53iVImuflrzw1weHEDKZhk/view?pli=1

Heaton, T. H., Hall, J. F., Wald, D. J., and Halling, M. W., 1995. Response of High-Rise and Base-Isolated Buildings to a Hypothetical Mw 7.0 Blind Thrust Earthquake. *Science*, **267**(5195), 206–211. DOI: 10.1126/science.267.5195.206

Hisada, Y., and Tanaka, S., 2021. What Is Fling Step? Its Theory, Simulation Method, and Applications to Strong Ground Motion near Surface Fault Ruptures. *Bulletin of the Seismological Society of America*. DOI: 10.1785/0120210046

Jia, Z., Jin, Z., Marchandon, M., Ulrich, T., Gabriel, A.-A., Fan, W., Shearer, P., et al., 2023. The complex dynamics of the 2023 Kahramanmaraş, Turkey, Mw 7.8-7.7 earthquake doublet. *Science*, **381**(6661), 985–990. DOI: 10.1126/science.adi0685

Kaneko, Y., and Goto, H., 2022. The Origin of Large, Long-Period Near-Fault Ground Velocities During Surface-Breaking Strike-Slip Earthquakes. *Geophysical Research Letters*, **49**(10), e2022GL098029. DOI: 10.1029/2022GL098029

Kobayashi, H., Koketsu, K., and Miyake, H., 2019. Rupture process of the 2018 Hokkaido Eastern Iburi earthquake derived from strong motion and geodetic data. *Earth, Planets and Space*, 71(1), 63. DOI: 10.1186/s40623-019-1041-7

Lin, Y.-Y., Kanamori, H., Zhan, Z., Ma, K.-F., and Yeh, T.-Y., 2020. Modelling of pulse-like velocity ground motion during the 2018 Mw 6.3 Hualien earthquake, Taiwan. *Geophysical Journal International*, **223**(1), 348–365. DOI: 10.1093/gji/ggaa306

Luzi L., Lanzano G., Felicetta C., D'Amico M. C., Russo E., Sgobba S., Pacor, F., & ORFEUS Working Group 5 (2020). Engineering Strong Motion Database (ESM) (Version 2.0). Istituto Nazionale di Geofisica e Vulcanologia (INGV), doi: https://doi.org/10.13127/ESM.2

Mai, P. M., Aspiotis, T., Aquib, T. A., Cano, E. V., Castro-Cruz, D., Espindola-Carmona, A., Li, B., et al., 2023. The Destructive Earthquake Doublet of 6 February 2023 in South-Central Türkiye and Northwestern Syria: Initial Observations and Analyses. *The Seismic Record*, **3**(2), 105–115. DOI: 10.1785/0320230007

Mena, B., and Mai, P. M., 2011. Selection and quantification of near-fault velocity pulses owing to source directivity. *Georisk: Assessment and Management of Risk for Engineered Systems and Geohazards*, **5**(1), 25–43. DOI: 10.1080/17499511003679949

Miyake, H., Koketsu, K., Hikima, K., Shinohara, M., and Kanazawa, T., 2010. Source Fault of the 2007 Chuetsu-oki, Japan, Earthquake. *Bulletin of the Seismological Society of America*, **100**(1), 384–391. DOI: 10.1785/0120090126

Paolucci, R., Pacor, F., Puglia, R., Ameri, G., Cauzzi, C., and Massa, M., 2011. Record processing in ITACA, the New Italian Strong-Motion Database. *Earthquake Data in Engineering Seismology, Geotechnical, Geological, and Earthquake Engineering* (Vol. 14, pp. 99–113). DOI: 10.1007/978-94-007-0152-6_8

Petersen, G. M., Büyükakpinar, P., Vera Sanhueza, F. O., Metz, M., Cesca, S., Akbayram, K., Saul, J., et al., 2023. The 2023 Southeast Türkiye Seismic Sequence: Rupture of a Complex Fault Network. *The Seismic Record*, **3**(2), 134–143. DOI: 10.1785/0320230008

Poiata, N., Miyake, H., and Koketsu, K., 2017. Mechanisms for Generation of Near-Fault Ground Motion Pulses for Dip-Slip Faulting. *Pure and Applied Geophysics*, **174**. DOI: 10.1007/s00024-017-1540-z

Poulos, A., and Miranda, E., 2023. Effect of Style of Faulting on the Orientation of Maximum Horizontal Earthquake Response Spectra. *Bulletin of the Seismological Society of America*, 113 (5): 2092–2105. DOI: 10.1785/0120230001

Rodriguez-Marek, A., and Bray, J. D., 2006. Seismic Site Response for Near-Fault Forward Directivity Ground Motions. *Journal of Geotechnical and Geoenvironmental Engineering*, **132**(12), 1611–1620. DOI: 10.1061/(ASCE)1090-0241(2006)132:12(1611)

Sengör A. M. C., Gorur N., Saroglu F., 1985. Strike-slip faulting and related basin formation in zones of tectonic escape: Turkey as a case study. *Society of Economic Paleontologists and Mineralogists, Special Publication* 37: 227 - 264

Shahi, S. K., and Baker, J. W., 2011. An Empirically Calibrated Framework for Including the Effects of Near-Fault Directivity in Probabilistic Seismic Hazard Analysis. *Bulletin of the Seismological Society of America*, **101**(2), 742–755. DOI: 10.1785/0120100090

Shahi, S. K., and Baker, J. W., 2014. An Efficient Algorithm to Identify Strong-Velocity Pulses in Multicomponent Ground Motions. *Bulletin of the Seismological Society of America*, **104**(5), 2456–2466. DOI: 10.1785/0120130191

Sharbati, R., Rahimi, R., Koopialipoor, M. R., Elyasi, N., Khoshnoudian, F., Ramazi, H. R., and Amindavar, H. R., 2020. Detection and extraction of velocity pulses of near-fault ground motions using asymmetric Gaussian chirplet model. *Soil Dynamics and Earthquake Engineering*, **133**, 106123. DOI: 10.1016/j.soildyn.2020.106123

Somerville, P. G., 2003. Magnitude scaling of the near fault rupture directivity pulse. *Physics of the Earth and Planetary Interiors*, **137**(1), 201–212. DOI: 10.1016/S0031-9201(03)00015-3

Somerville, P. G., Smith, N. F., Graves, R. W., and Abrahamson, N. A., 1997. Modification of Empirical Strong Ground Motion Attenuation Relations to Include the Amplitude and Duration Effects of Rupture Directivity. *Seismological Research Letters*, **68**(1), 199–222. DOI: 10.1785/gssrl.68.1.199

Strasser, F. O., and Bommer, J. J., 2009. Review: Strong Ground Motions—Have We Seen the Worst? *Bulletin of the Seismological Society of America*, **99**(5), 2613–2637. DOI: 10.1785/0120080300

Tatar, O., Piper, J. D. A., Gürsoy, H., Heimann, A., & Koçbulut, F., 2004. Neotectonic deformation in the transition zone between the Dead Sea Transform and the East Anatolian Fault Zone, Southern Turkey: a palaeomagnetic study of the Karasu Rift Volcanism. *Tectonophysics*, 385(1-4), 17-43.

Türker, E., Yen, M., Pilz, M., and Cotton, F., 2023. Significance of Pulse-Like Ground Motions and Directivity Effects in Moderate Earthquakes: The Example of the Mw 6.1 Gölyaka-Düzce Earthquake on 23 November 2022. *Bulletin of the Seismological Society of America*, XX, 1–10. DOI: 10.1785/0120230043

Yen, M.-H., von Specht, S., Lin, Y.-Y., Cotton, F., and Ma, K.-F., 2022. Within- and Between-Event Variabilities of Strong-Velocity Pulses of Moderate Earthquakes within Dense Seismic Arrays. *Bulletin of the Seismological Society of America*, **112**(1), 361–380. DOI: 10.1785/0120200376

Zhu, L., and L. A. Rivera, 2002. A note on the dynamic and static displacements from a point source in multilayered media, *Geophys. J. Int.* **148(3)**, 619–627. DOI: 10.1046/j.1365-246X.2002.01610.x

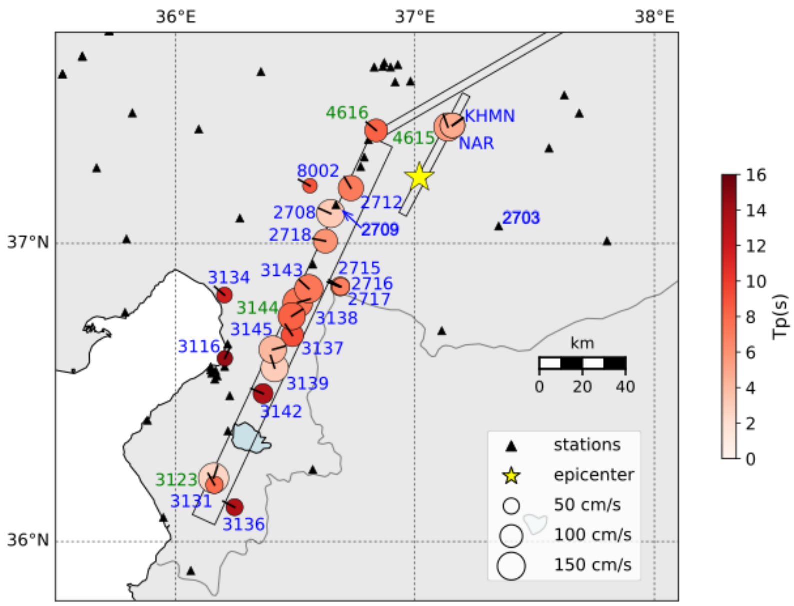

(a)

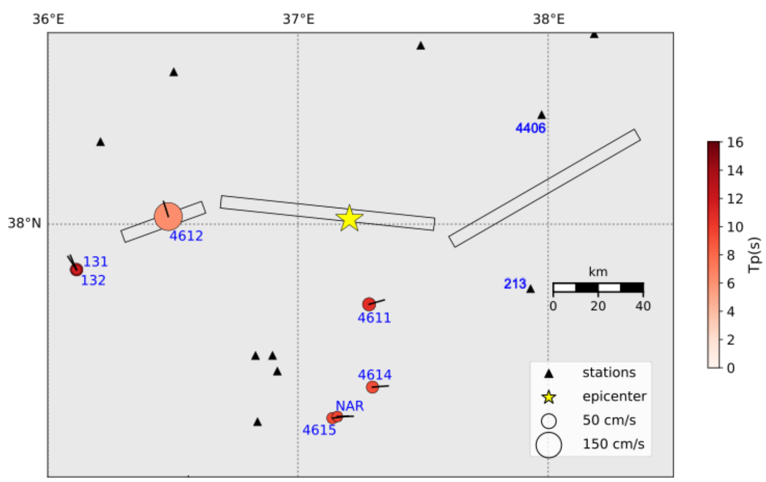

(b)

Figure 1. Distributions of the strongest velocity pulses detected for (a) the Mw 7.8 Pazarcik earthquake, and (b) the Mw 7.5 Elbistan earthquake from the corrected observation dataset. The circles represent the velocity pulses identified in the events. The size of the circles represents the amplitude of the velocity pulses. The color in the circles represents the pulse period, Tp. The arrows on the circles represent the orientations of the strongest pulses. Fault geometries are from USGS. The station names with color green are the stations shown in **Figure 2**, **S1**, and **S2**.

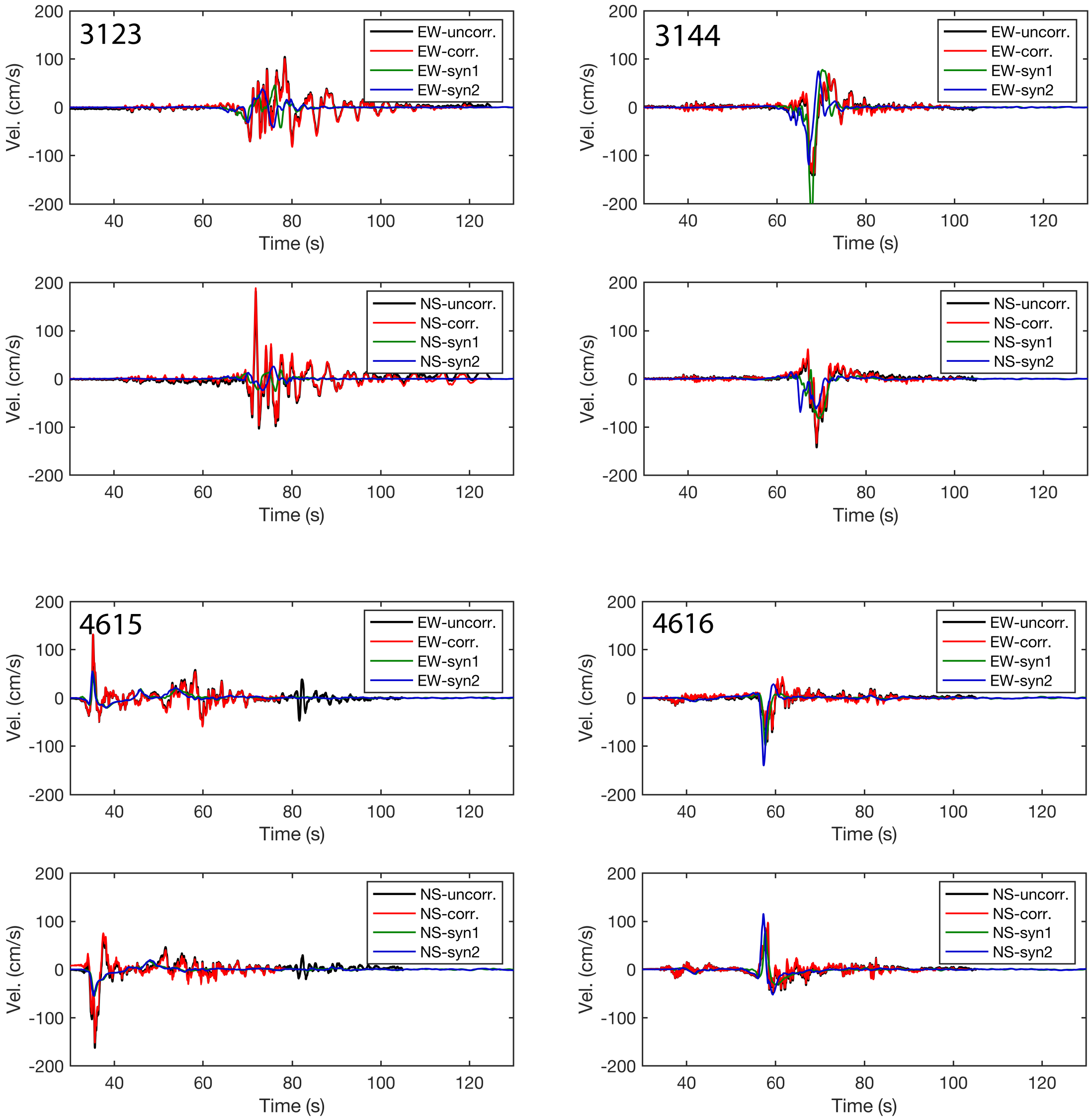

Figure 2. Comparison of velocity time histories on the EW and NS components for the uncorrected (uncorr.), corrected (corr.), 1st synthetic data (syn1), and 2nd synthetic data (syn2) for the Mw 7.8 Pazarcik earthquake. The geographic locations of the stations (names in green) are shown in **Figure 1**.

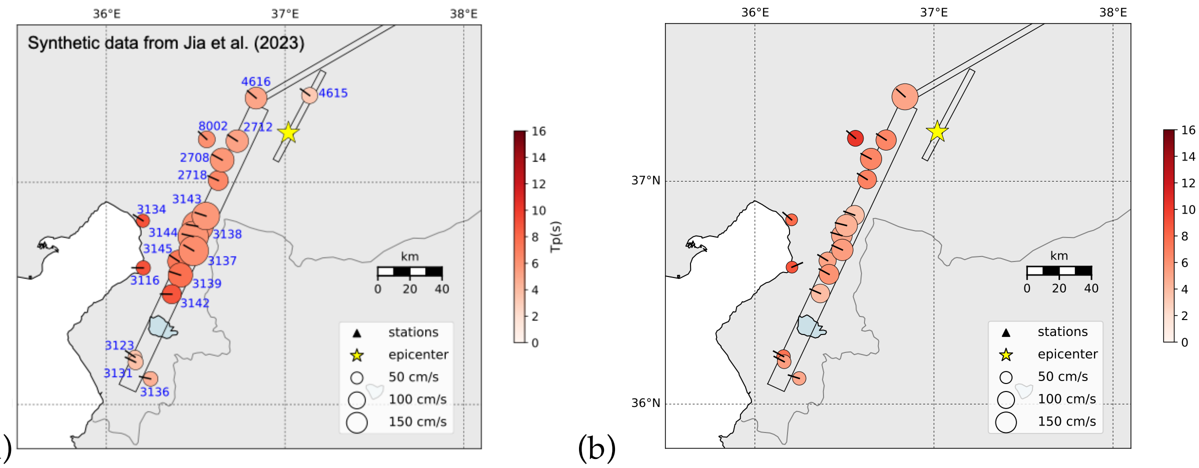

(a) (b)

Figure 3. Distributions of the strongest velocity pulses detected from (a) simulations (Jia et al. 2023) and (b) simulations from the model of Jia et al. (2023) in higher resolution (numerically accurate to 5 Hz) for the Mw 7.8 Pazarcik earthquake. The circles represent the velocity pulses identified in the events. The size of the circles represents the amplitude of the velocity pulses. The color in the circles represents the pulse period, Tp. The arrows on the circles represent the orientations of the strongest pulses. Fault models are from geometries are from USGS.

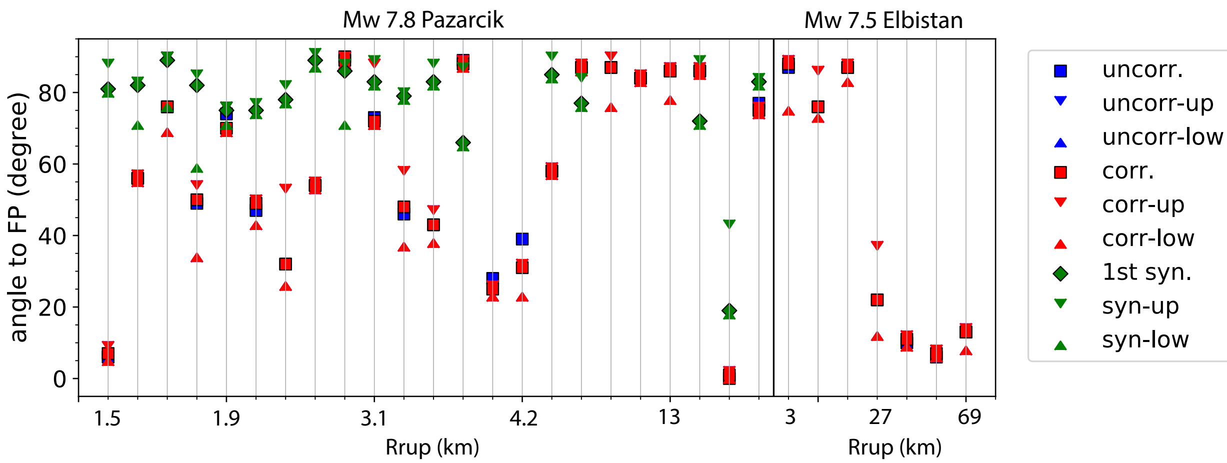

Figure 4. Comparison of the pulse orientations with the maximum and minimum values from the uncorrected data (blue squares), corrected data (red squares) and 1st synthetic data (green squares) of two earthquakes. The left panel is the first event, and the right panel is the second event.

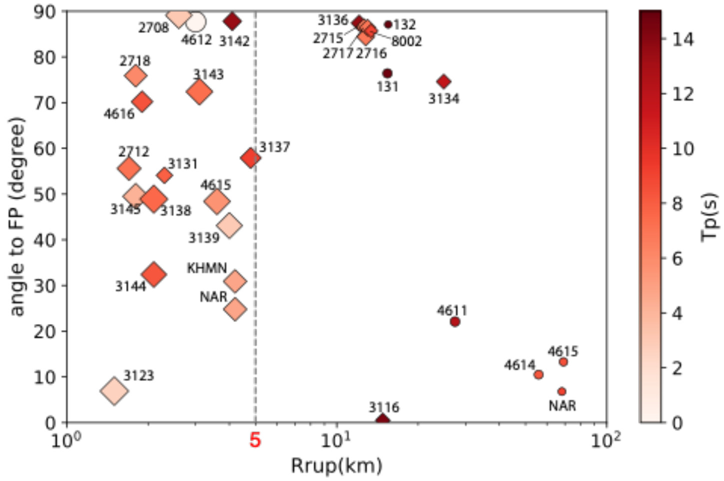

(a)

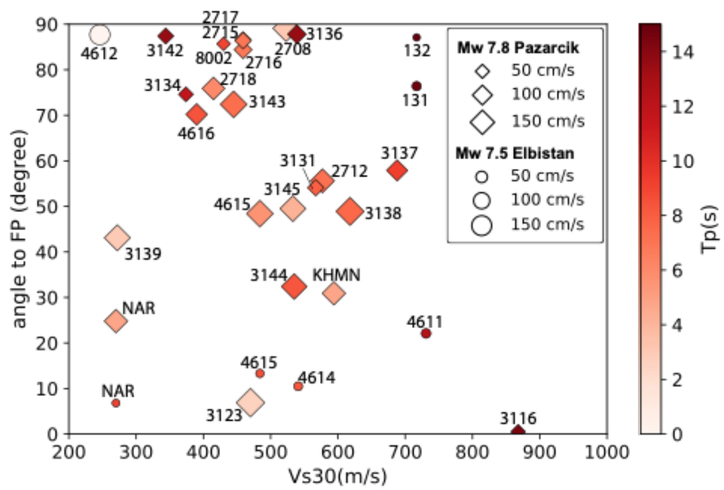

(b)

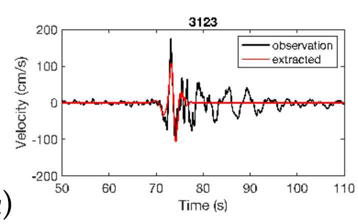

(c)

Figure 5. (a)Pulse periods, velocity, the angles to the FP component as a function of the rupture distance for the strongest pulses from the corrected data. (b)Pulse period, velocity, and angle to FP with Vs30 for the strongest pulses from the corrected data. The diamonds indicate the pulses of the Mw 7.8 Pazarcik earthquake. The circles indicate the pulses of the Mw 7.5 Elbistan earthquake. The color represents the pulse periods. (c) A rotated time history of pulse induced by the soft-soil effect at station 3123.

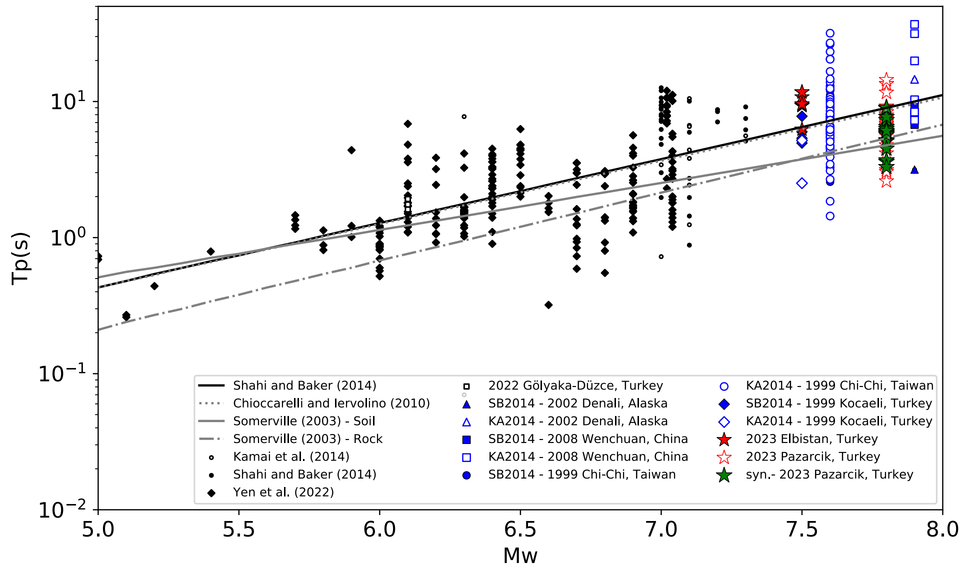

Figure 6. Values of the pulse period, Tp, as a function of earthquake moment magnitude. The lines show the regressions of Shahi and Baker (2014), black solid line, Chioccarelli and Iervolino (2010), grey dotted line and Somerville (2003), grey dashed-dotted-dashed line. Black dots represent the pulses identified from the NGA-West2 database (Ancheta et al., 2014) in the study of Shahi and Baker (2014). Open circles represent the fling-step pulses published by Kamai et al. (2014). Figure modified and adapted from Yen et al., (2022). Red stars represent the pulses of this earthquake doublet. Green stars represent the pulses of this earthquake doublet from the 1st synthetic data.

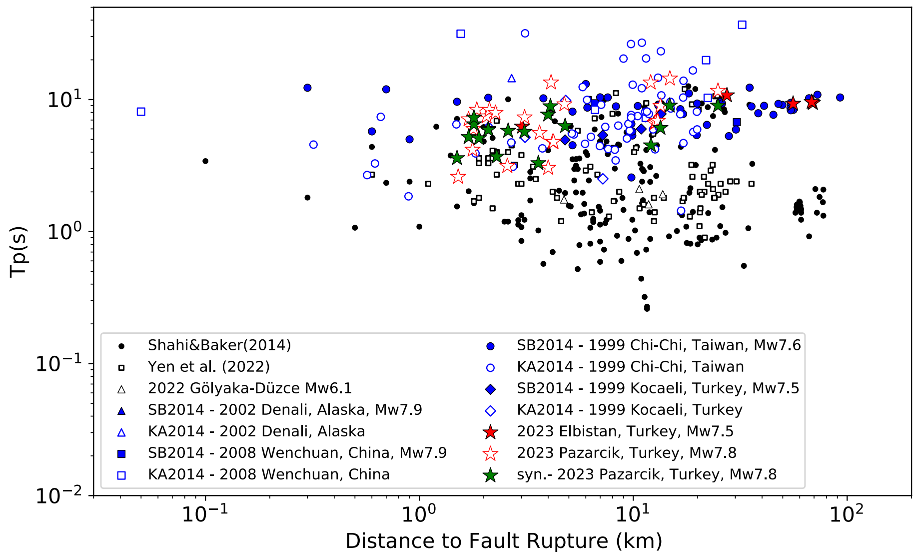

(a)

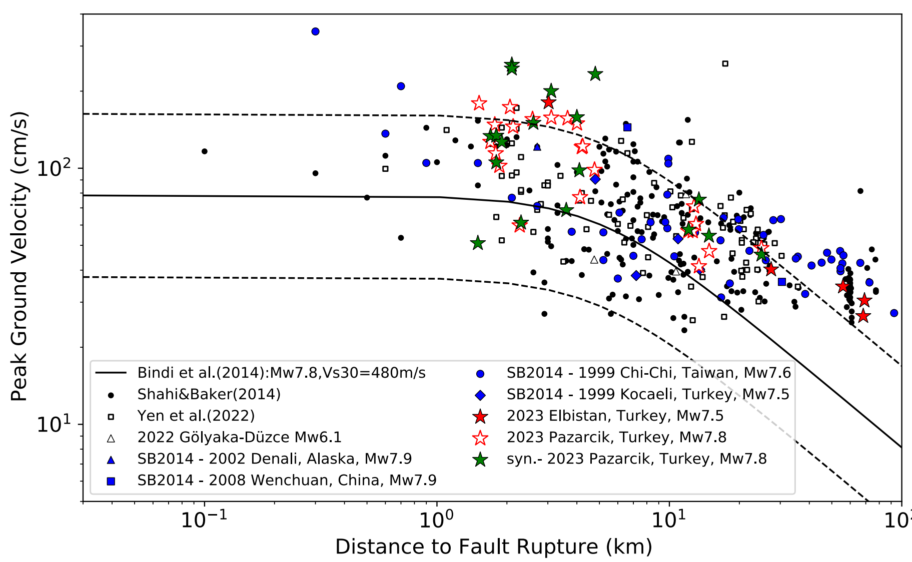

(b)

Figure 7. Scaling of (a) pulse period, Tp and (b) pulse PGV, as a function of distance to fault rupture. Black dots represent the pulses identified from the NGA-West2 database (Ancheta et al., 2014) in the study by Shahi and Baker (2014) for the M<7.5 earthquakes. Open squares indicate the pulses published by Yen et al. (2022) for which the static offset of the events has been removed. The solid line in (b) represents the predicted ground velocities from the ground motion model of Bindi et al. (2014) for Mw7.8 and Vs30 = 480 m/s. The dashed lines represent one standard deviation of the median of the predicted ground velocities.

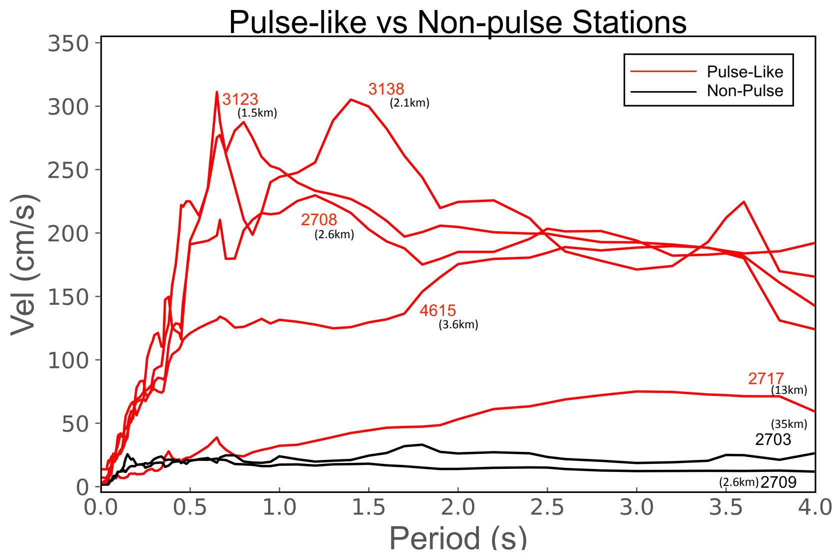

(a)

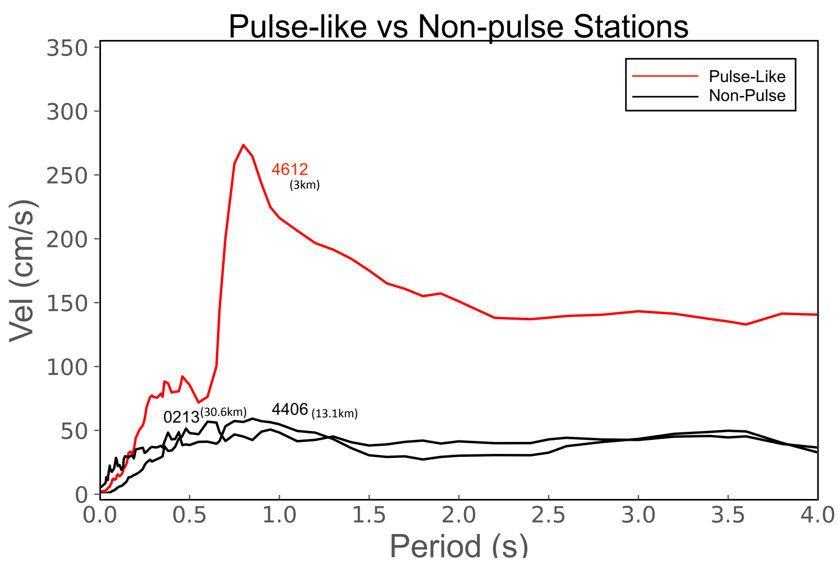

(b)

Figure 8. A selection of velocity response spectra of the observations for the strong pulses (PI>10) for (a) the Mw 7.8 Pazarcik and (b) the Mw 7.5 Elbistan earthquakes. Red curves show the velocity response spectra of stations with a pulse-like feature. Black curves show the velocity response spectra of stations with a non-pulse-like feature.

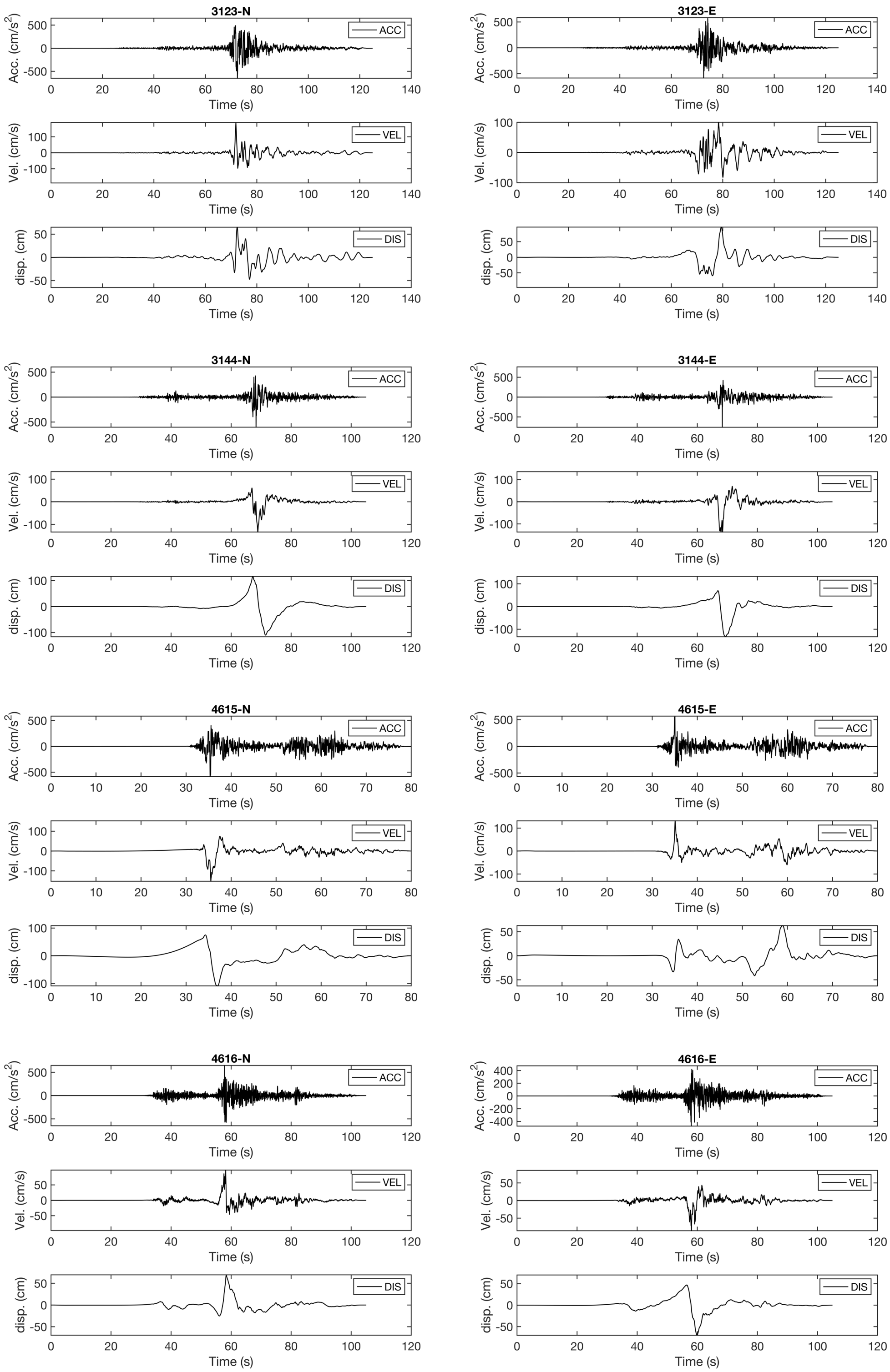

Figure S1. Acceleration, velocity, and displacement time histories on the EW and NS components for the corrected data for the Mw 7.8 Pazarcik earthquake. The geographic locations of the stations (names in green) are shown in **Figure 1**.

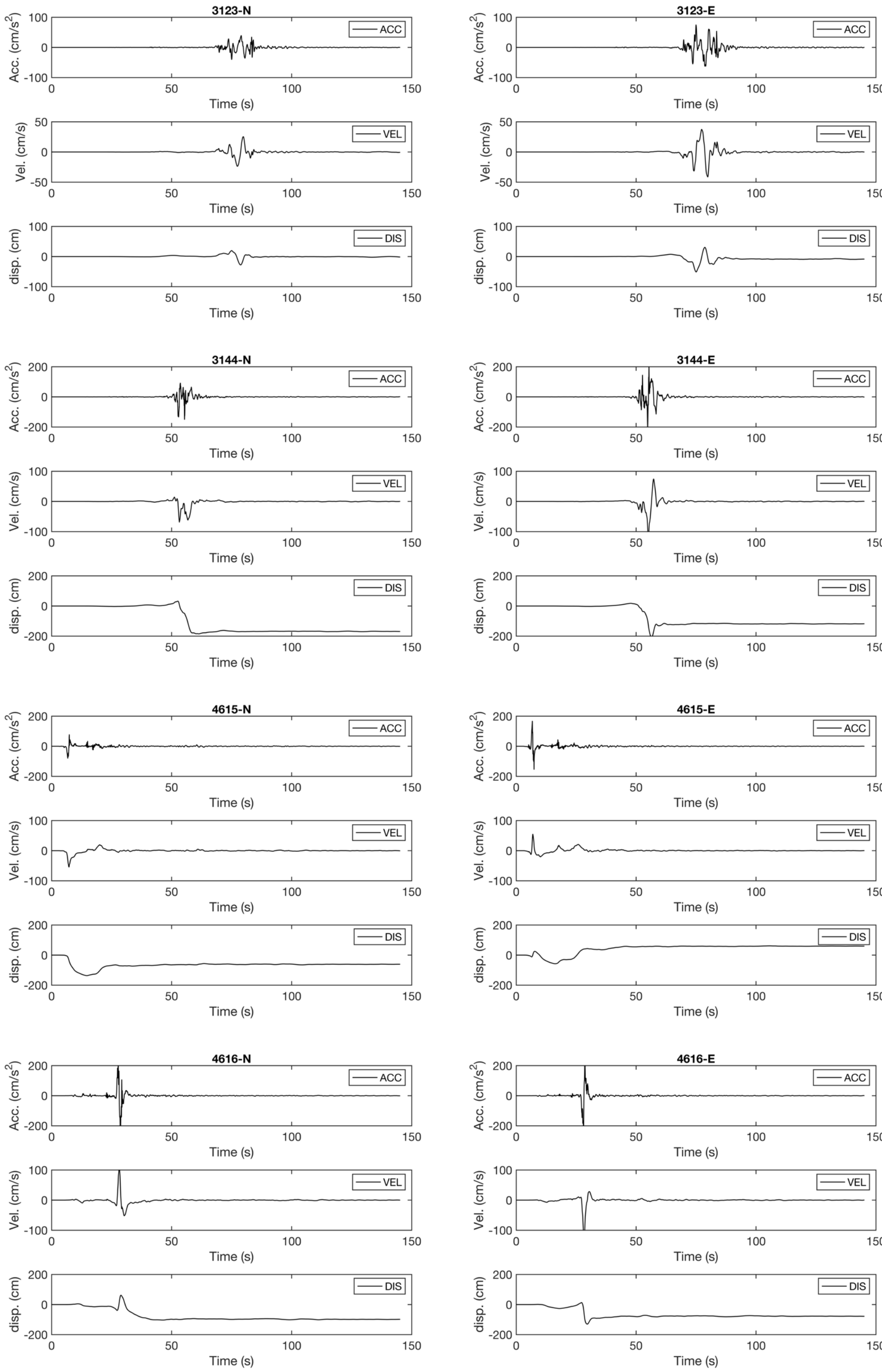

Figure S2. Acceleration, velocity, and displacement time histories on the EW and NS components for the 1st generation synthetic data for the Mw 7.8 Pazarcik earthquake from the dynamic rupture simulation. The geographic locations of the stations (names in green) are shown in **Figure 1**.

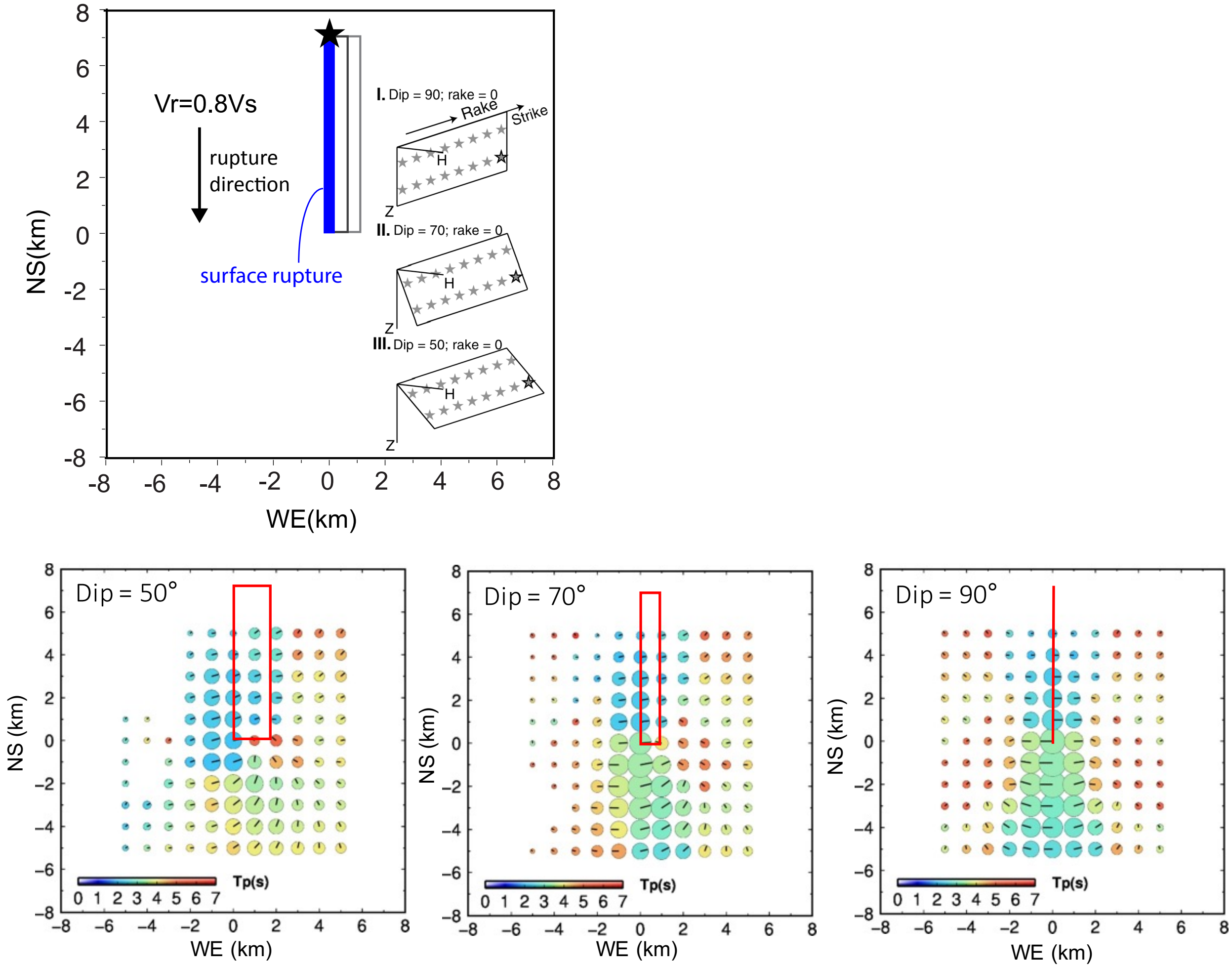

Figure S3. The kinematic simulations based on the f-k approach (Zhu and Rivera, 2002). These simulations focus on the near-fault region of earthquake (M6) for analyzing the impact of the fault mechanism on the pulse characteristics. The upper panel shows the setting of the simulations. The rupture velocity (Vr) is set at 2.4 km/s (0.8 times the S-wave velocity [VS], 3.0 km/s). The star indicates the initial rupture point. The velocity structure is referred to the velocity model of Lin et al. (2020) for hard-rock site conditions. The lower panel shows the distribution of the pulses for various fault dipping (50°, 70°, and 90°). The circle color represents the pulse period, and the size of the circle represents the pulse velocity. The arrow in the circle indicates the pulse orientation.

Table 1. Parameters table of the extracted pulses for the Mw7.8 Pazarcik earthquake. R_{hypo}, distance to the hypocenter; R_{rup}, distance to the rupture plane; Ang., angle to the fault-parallel component. Ori., orientation of the strongest observed pulse, in degrees clockwise from north; PGV, peak ground velocity of the strongest observed pulse; and T_P, the period of the extracted pulse in the direction of the strongest observed pulse.

index	Sta.	R_{hypo} (km)	R_{rup} (km)	uncorrected data					corrected data					1st synthetic data					2nd synthetic data				
				Ang.	Ori.	T_p (s)	PGV (cm/s)	PI	Ang.	Ori.	T_p (s)	PGV (cm/s)	PI	Ang.	Ori.	T_p (s)	PGV (cm/s)	PI	Ang.	Ori.	T_p (s)	PGV (cm/s)	PI
1	3123	133.1	1.5	6	19	2.6	172.8	14.4	7	18	2.6	179.2	20.0	81	-56	3.6	51.0	3.8	87	-62	7.6	48.5	6.9
2	2712	32.8	1.7	56	-31	7.0	128.3	7.1	56	-31	7.1	126.7	7.5	82	-57	5.2	133.6	35.7	82	-57	6.6	109.0	25.2
3	2718	44.6	1.8	76	-79	6.0	134.0	7.9	76	-79	6.0	114.4	23.1	89	-66	6.5	105.4	26.8	83	-58	6.8	92.7	19.3
4	3145	82.9	1.8	49	74	4.2	147.5	23.0	50	75	4.2	147.9	24.4	82	-57	7.3	134.0	37.0	84	-59	5.1	78.3	15.3
5	4616	34.5	1.9	74	-49	8.4	104.9	10.9	70	-50	8.4	102.2	11.9	75	-50	5.1	126.7	19.5	73	-48	5.1	180.5	33.9
6	3138	64.6	2.1	47	72	7.9	184.3	12.3	49	74	7.5	173.2	25.0	75	-80	6.0	253.5	36.5	79	-76	4.5	127.8	19.9
7	3144	69.5	2.1	32	57	8.3	153.9	11.9	32	57	8.3	145.4	15.0	78	-77	5.9	245.0	42.1	81	-74	5.1	112.5	24.7
8	3131	134.9	2.3	54	-29	8.0	57.2	1.0	54	-29	7.9	59.8	4.6	89	-64	3.7	61.3	9.1	87	-62	5.5	49.9	9.2
9	2708	39.9	2.6	90	-65	3.2	172.4	5.2	89	-66	3.1	155.4	15.9	86	-61	5.8	150.3	43.3	87	-62	6.6	119.9	32.3
10	3143	58.5	3.1	73	-48	7.2	165.6	20.9	72	-47	7.3	157.6	24.6	83	-72	5.7	200.1	34.5	85	-70	3.7	99.8	1.9
11	4615	31.5	3.6	46	-21	5.5	166.0	23.9	48	-20	5.6	156.6	27.8	79	-54	3.3	68.6	3.0	-	-	-	-	-
12	3139	87.3	4.0	43	-18	3.1	151.8	19.8	43	-18	3.0	149.6	23.3	83	-72	7.7	158.2	15.9	87	-62	6.0	104.1	16.9
13	3142	97.2	4.1	89	-66	13.8	80.7	2.5	88	-67	13.5	77.1	0.6	66	-89	8.9	98.1	10.0	88	-67	3.9	91.7	16.4
14	NAR	32.5	4.2	28	53	4.8	125.7	19.2	25	53	4.8	121.8	20.8	-	-	-	-	-	-	-	-	-	-
15	KHMN	32.5	4.2	39	64	5.2	99.1	8.3	31	56	4.8	120.9	20.0	-	-	-	-	-	-	-	-	-	-
16	3137	74.2	4.8	58	-33	9.3	103.3	18.5	58	-33	9.2	98.5	18.5	85	-60	6.3	233.2	39.1	89	-66	5.5	121.4	28.9
17	3136	137.8	12.1	87	-62	11.5	58.1	1.7	87	-62	13.5	56.9	1.4	77	-78	4.5	57.6	6.1	82	-73	5.0	47.9	7.8
18	2715	50.1	12.6	87	-68	7.0	76.2	0.5	87	-68	6.6	56.8	13.3	-	-	-	-	-	-	-	-	-	-
19	2716	49.9	12.8	84	-59	6.9	73.5	7.5	84	-59	6.8	71	8.9	-	-	-	-	-	-	-	-	-	-

20	2717	49.8	13.0	86	-69	7.0	62.9	10.5	86	-69	6.9	60.6	11.6	-	-	-	-	-	-	-	-	-	-
21	8002	46.2	13.4	86	-61	9.2	42.8	3.3	86	-61	9.0	41.4	3.8	72	-47	6.1	75.4	14.7	75	-50	10.3	67.4	12.4
22	3116	97.9	14.8	0	25	15.1	49.9	7.1	1	26	14.4	47.5	6.4	66	-89	9.0	54.5	10.3	42	67	8.9	36.9	4.3
23	3134	85.2	24.9	77	-52	11.9	50.7	5.2	75	-50	11.7	48.7	4.2	83	-58	9.0	46.0	4.9	74	-49	7.9	37.4	1.4

Table 2. Parameters table of the extracted pulses for the Mw7.5 Elbistan earthquake.

index	Sta.	R_{hypo} (km)	R_{rup} (km)	uncorrected data					corrected data				
				Ang.	Ori.	T_p (s)	PGV (cm/s)	PI	Ang.	Ori.	T_p (s)	PGV (cm/s)	PI
24	4612	64.0	3.0	87	-17	6.2	181.4	13.9	88	-18	6.2	180.9	13.7
25	131	97.7	15.4	76	-34	12.2	38.2	3.8	76	-34	11.7	37.4	4.0
26	132	97.7	15.5	87	-23	12	25.1	1.3	87	-23	11.8	24.2	1.0
27	4611	33.1	27.4	22	74	11	42.5	4.5	22	74	10.8	40.3	4.3
28	4614	61.3	55.9	10	86	9.3	34.2	3.5	11	86	9.3	34.5	3.7
29	NAR	71.1	68.2	6	90	9.7	27.9	2.6	7	89	9.6	26.5	2.2
30	4615	71.8	69.1	13	83	9.4	30.8	3.3	13	83	9.4	30.4	3.3